Non-conforming Finite Elements for Flexible Discretization with Applications to Aeroacoustics

Manfred Kaltenbacher

Abstract The non-conforming Finite Element (FE) method allows the coupling of two or more sub-domains with quite different mesh sizes. Therewith, we gain the flexibility to choose for each sub-domain an optimal grid. The two proposed methods - Mortar and Nitsche-type mortaring - fulfill the physical conditions along the non-conforming interfaces. We exploit this capability and apply it to real engineering applications in aeroacoustics. The results clearly demonstrate the superiority of the non-conforming FE method over the standard FE method concerning pre-processing, mesh generation flexibility, accuracy and computational time.

1 Overview

For low Mach number flows, the speed of sound is much greater than the mean flow velocity and therefore the acoustic wavelength is much greater than the diameters of the eddies in the flow. Therefore, the only practicable approach for such cases to compute flow induced sound, known as computational aeroacoustics, is based on hybrid methods (Kaltenbacher et al. 2010). These methods compute the flow on a restricted sub-domain in a first step applying, e.g., Large Eddy Simulation (LES) to accurately resolve the main turbulent flow structures. In a subsequent step, the acoustic wave propagation within this sub-domain as well as in an ambient surrounding sub-domain is computed. The main approaches for this step are solving the linearized Euler equations, the acoustic perturbation equations, the linearized perturbed compressible equations or Lighthill's inhomogeneous wave equation (Kaltenbacher 2015). All these methods have in common, that they compute within the flow domain acoustic source terms based on the flow computation (Computational Fluid Dynamics, CFD). In order to accurately resolve these source terms, a much finer discretization is needed in the flow domain as in the ambient domain of free wave radiation.

M. Kaltenbacher (✉)
Institute of Mechanics and Mechatronics, TU Wien, Vienna, Austria
e-mail: manfred.kaltenbacher@tuwien.ac.at

M. Kaltenbacher (ed.), *Computational Acoustics*, CISM International Centre for Mechanical Sciences 579, DOI 10.1007/978-3-319-59038-7_2

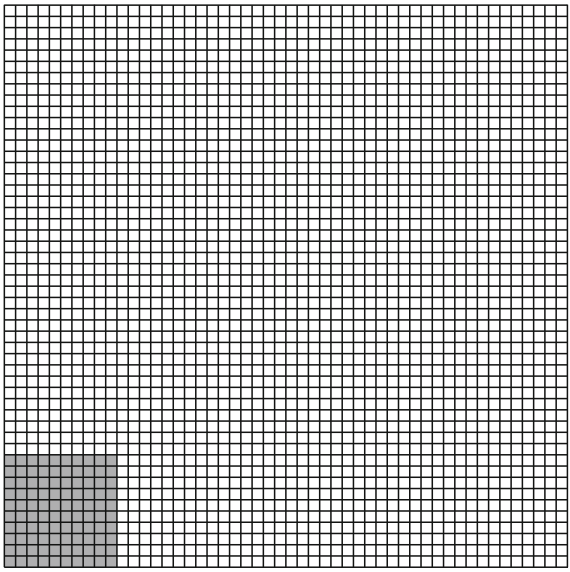

Fig. 1 Uniform mesh

The simplest approach to resolve the different grid sizes is to keep the fine discretization necessary for one sub-domain also for the other sub-domain (cf. Fig. 1). However, in many cases, a tremendous number of unknowns is obtained, so that a solution even on high performance computers is not feasible. In a second approach, the mesh could be gradually coarsened as in Fig. 2. Quite often this is the only possible choice, if the standard conforming FE method is used, since it can only handle a geometrically conforming triangulation. Unfortunately, the numerical accuracy of wave propagation applications depend very sensitively on the shape regularity of the underlying mesh. Thus, a small transition zone from fine to coarse grids results in a poor numerical approximation. Therefore, in order to meet the requirements of different mesh sizes and to gain full flexibility for the discretization, we propose to use the non-conforming FE method. More precisely the mesh-size ratio does not enter into the a priori error estimates. Using this approach, one gains much more flexibility in the modeling, since specially tuned meshes for the subproblems can be used. Most important is that the proposed formulations fulfill the physical interface conditions. Therefore, the advantages can be summarized as follows (Fig. 3):

- Pre-processing is much more flexible, since grids in the different sub-domains do not influence each other. Depending on the implementation, the global mesh may be read in parts from multiple mesh input files. This makes parameter studies handy to conduct.
- The approximation order can be chosen independently for each sub-domain. This permits to use higher order elements in regions, where the solution is known to be smooth and fine discretizations using low order elements may be used in regions, where singularities in the solution occur.

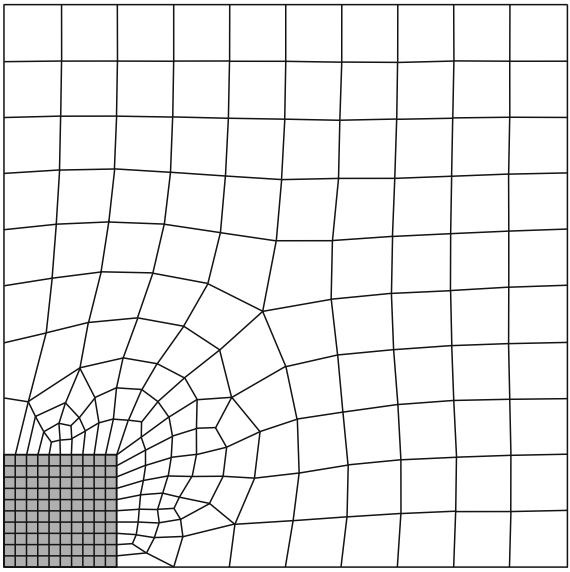

Fig. 2 Coarsening mesh

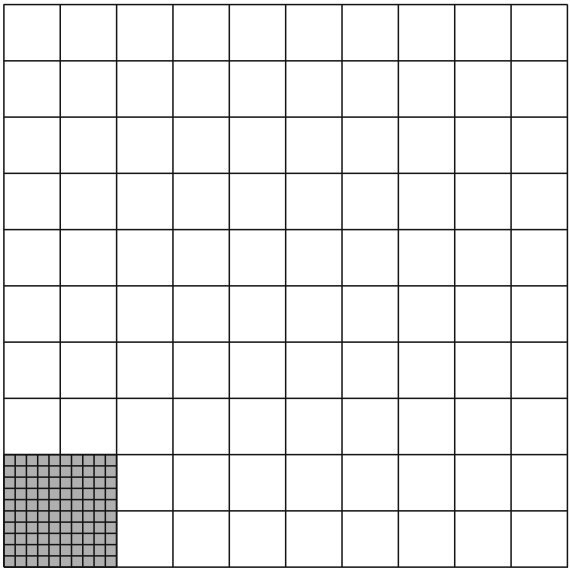

Fig. 3 Non-conforming mesh

- The method can be used for parallelization. If only a single physical field is involved, our method can be classified as a Finite Element Tearing and Interconnection dual-primal (FETI-DP) method in domain decomposition terms, see, e.g., Langer and Steinbach (2003), Dokeva (2006).

Here, we focus on computational aeroacoustics and discuss formulations and applications in case of acoustic-acoustic coupling. However, we want to note that non-conforming grid techniques are applicable to domain coupling field problems, e.g. vibro-acoustics (Flemisch et al. 2012), fluid-structure-interaction (Klöppel et al. 2011), electro-thermal coupling (Köck et al. 2015).

The non-conforming grid techniques have been implemented in our multiphysics research software CFS++ (see cfs-doc.mdmt.tuwien.ac.at), and used for the computations of the applications described in Sect. 5.

2 Non-conforming FE Formulations

We will investigate two approaches to handle non-conforming grids: (1) Mortar coupling, see, e.g., Bernardi et al. (1994), Wohlmuth (2000) and (2) Nitsche-type coupling, see, e.g., Hansbo et al. (2003), Fritz et al. (2004). In the first approach, we guarantee the strong coupling of the numerical flux (normal derivative of the acoustic pressure) by introducing a Lagrange multiplier and coupling of the acoustic pressure in a weak sense. Nitsche-type coupling does not need the additional Lagrange multiplier and handles the coupling by symmetrizing the bilinear form and adding a special jump term.

We assume a global domain Ω and its decomposition into two sub-domains Ω_1, Ω_2 as displayed in Fig. 4. Thus, in each sub-domain we solve the wave equation for the acoustic pressure $p_{ai} : \Omega_i \times (0, T) \to \mathrm{IR}$,

$$\frac{1}{c^2}\,\ddot{p}_{ai} - \Delta\, p_{ai} = g_i, \quad \text{in } \Omega_i \times (0, T),\ i = 1, 2 \tag{1}$$

completed by appropriate initial conditions at time $t = 0$ and boundary conditions on the global boundary Γ_a. In (1) a dot over a variable denotes the derivative with respect to time, i.e. $\ddot{p}_a = \partial^2 p_a / \partial t^2$. According to the physical interface conditions, we have to impose continuity for trace and flux of the acoustic pressure along the common interface Γ_I, i.e.,

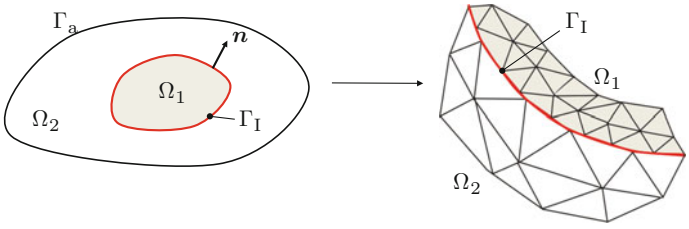

Fig. 4 Acoustic domain with two sub-domains Ω_1 and Ω_2 with different discretizations

$$p_{\mathrm{a}1} = p_{\mathrm{a}2} \quad \text{and} \quad \frac{\partial p_{\mathrm{a}1}}{\partial \boldsymbol{n}} = \frac{\partial p_{\mathrm{a}2}}{\partial \boldsymbol{n}} \quad \text{on} \quad \Gamma_{\mathrm{I}} \,. \tag{2}$$

Without any limitation and to keep the focus on the main steps achieving non-conforming FE formulations, we set homogeneous Dirichlet boundary condition for the acoustic pressure p_{a} at Γ_{a}.

2.1 Mortar Formulation

The flux coupling condition is enforced in a strong sense by introducing a Lagrange multiplier

$$\lambda = -\frac{\partial p_{\mathrm{a}1}}{\partial \boldsymbol{n}} = -\frac{\partial p_{\mathrm{a}2}}{\partial \boldsymbol{n}} \,. \tag{3}$$

However, the continuity of the trace will be understood in a weak sense

$$\int_{\Gamma_{\mathrm{I}}} (p_{\mathrm{a}1} - p_{\mathrm{a}2}) \mu \, \mathrm{d}\boldsymbol{s} = 0 \tag{4}$$

for all test functions μ out of a suitable Lagrange multiplier space. We proceed with the weak formulation and obtain from (1)

$$\int_{\Omega_i} \frac{1}{c^2} \, w_i \, \ddot{p}_{\mathrm{a}i} \, \mathrm{d}\boldsymbol{x} + \int_{\Omega_i} \nabla w_i \cdot \nabla p_{\mathrm{a}i} \, \mathrm{d}\boldsymbol{x} - \int_{\Gamma_{\mathrm{I}}} w_i \, \boldsymbol{n}_i \cdot \nabla p_{\mathrm{a}i} \, \mathrm{d}\boldsymbol{s} = \int_{\Omega_i} w_i \, g_i \, \mathrm{d}\boldsymbol{x} \,,$$

for all test functions w_i, $i = 1, 2$. Please note that the surface term

$$\int_{\Gamma_{\mathrm{a}}} w_2 \, \boldsymbol{n}_{\mathrm{a}} \cdot \nabla p_{\mathrm{a}2} \, \mathrm{d}\boldsymbol{s}$$

vanishes, since the test function is zero at Dirichlet boundaries of p_{a}. Inserting the definition of the Lagrange multiplier (3) and summing up, we obtain the symmetric evolutionary saddle point problem of finding $p_{\mathrm{a}1}$, $p_{\mathrm{a}2}$ and λ such that

$$\sum_{i=1}^{2} \left(\int_{\Omega_i} \frac{1}{c^2} w_i \, \ddot{p}_{\mathrm{a}i} \, \mathrm{d}\boldsymbol{x} + \int_{\Omega_i} \nabla w_i \cdot \nabla p_{\mathrm{a}i} \, \mathrm{d}\boldsymbol{x} \right) + \int_{\Gamma_{\mathrm{I}}} (w_1 - w_2) \lambda \, \mathrm{d}\boldsymbol{s} = \sum_{i=1}^{2} \int_{\Omega_i} w_i g_i \, \mathrm{d}\boldsymbol{x} \tag{5}$$

$$\int_{\Gamma_{\mathrm{I}}} (p_{\mathrm{a}1} - p_{\mathrm{a}2}) \mu \, \mathrm{d}\boldsymbol{s} = 0 \tag{6}$$

for all μ and w_i, $i = 1, 2$. We now face a primal-dual problem, where the coupling is realized in terms of Lagrange multipliers. In a next step, we perform a spatial discretization, assume the Lagrange multiplier to be chosen with respect to Ω_1 and choose the following ansatz

$$w_1 \approx w_1^h = \sum_i N_{1i}\, w_{1i}\,; \quad p_{\mathrm{a},1} \approx p_{\mathrm{a},1}^h = \sum_j N_{1j}\, p_{\mathrm{a},1,j} \tag{7}$$

$$w_2 \approx w_2^h = \sum_i N_{2i}\, w_{2i}\,; \quad p_{\mathrm{a},2} \approx p_{\mathrm{a},2}^h = \sum_j N_{2j}\, p_{\mathrm{a},2,j} \tag{8}$$

$$\lambda \approx \lambda^h = \sum_k \phi_k\, \lambda_k\,. \tag{9}$$

Substituting this ansatz into (5), (6), results in the semi-discrete Galerkin formulation, which reads as

$$\begin{pmatrix} \boldsymbol{M}_1 & 0 & 0 \\ 0 & \boldsymbol{M}_2 & 0 \\ 0 & 0 & 0 \end{pmatrix} \begin{pmatrix} \ddot{\underline{p}}_{\mathrm{a}1} \\ \ddot{\underline{p}}_{\mathrm{a}2} \\ \ddot{\underline{\lambda}} \end{pmatrix} + \begin{pmatrix} \boldsymbol{K}_1 & 0 & \boldsymbol{D} \\ 0 & \boldsymbol{K}_2 & \boldsymbol{M} \\ \boldsymbol{D}^T & \boldsymbol{M}^T & 0 \end{pmatrix} \begin{pmatrix} \underline{p}_{\mathrm{a}1} \\ \underline{p}_{\mathrm{a}2} \\ \underline{\lambda} \end{pmatrix} = \begin{pmatrix} \underline{f}_1 \\ \underline{f}_2 \end{pmatrix}. \tag{10}$$

In (10) $\boldsymbol{M}_i$ and $\boldsymbol{K}_i$ are the standard mass and stiffness matrices, see e.g. (Kaltenbacher 2015), $\underline{f}_i$ the algebraic vectors of the right hand side in Ω_i, and $\underline{p}_{\mathrm{a}1}$, $\underline{p}_{\mathrm{a}2}$, $\underline{\lambda}$ the algebraic vectors of the unknown acoustic pressures in Ω_1, Ω_2 and Lagrange multiplier along Γ_{I}, respectively. The coupling matrices $\boldsymbol{D}$, $\boldsymbol{M}$ are given by

$$\boldsymbol{D}^e = [\boldsymbol{D}_{pq}]; \quad \boldsymbol{D}_{pq} = \int_{\Gamma_{\mathrm{I}}} N_{1p}\phi_q \mathrm{d}\boldsymbol{s}, \tag{11}$$

$$\boldsymbol{M} = [\boldsymbol{M}_{pq}]; \quad \boldsymbol{M}_{pq} = \int_{\Gamma_{\mathrm{I}}} N_{2p}\phi_q \mathrm{d}\boldsymbol{s}, \tag{12}$$

where N_{1p} and N_{2p} denote the finite element basis functions on $\mathcal{T}_1$ and $\mathcal{T}_2$, respectively, and ϕ_q denotes the Lagrange multiplier basis function associated with node q. We note that the assembly of $\boldsymbol{D}$ poses no difficulty since all basis functions involved are defined with respect to the same grid $\mathcal{T}_1$. However, the assembly of $\boldsymbol{M}$ is more involved, since N_{2p} and ϕ_q are defined with respect to different grids (see Sect. 4).

2.2 Nitsche-Type Mortaring Formulation

To handle the non-conforming discretization within Nitsche's method, we start at the weak formulation for both sub-domains Ω_1 and Ω_2

$$\int_{\Omega_1} \frac{1}{c^2}\, w_1 \ddot{p}_{\mathrm{a}1} \mathrm{d}\boldsymbol{x} + \int_{\Omega_1} \nabla w_1 \cdot \nabla p_{\mathrm{a}1} \mathrm{d}\boldsymbol{x} - \int_{\Gamma_\mathrm{I}} w_1 \frac{\partial p_{\mathrm{a}1}}{\partial \boldsymbol{n}_1}\, \mathrm{d}\boldsymbol{s} = \int_{\Omega_1} w_1 g_1 \, \mathrm{d}\boldsymbol{x} \tag{13}$$

$$\int_{\Omega_2} \frac{1}{c^2}\, w_2 \ddot{p}_{\mathrm{a}2} \mathrm{d}\boldsymbol{x} + \int_{\Omega_2} \nabla w_2 \cdot \nabla p_{\mathrm{a}2} \mathrm{d}\boldsymbol{x} - \int_{\Gamma_\mathrm{I}} w_2 \frac{\partial p_{\mathrm{a}2}}{\partial \boldsymbol{n}_2}\, \mathrm{d}\boldsymbol{s} = \int_{\Omega_2} w_2 g_2 \, \mathrm{d}\boldsymbol{x} \,. \tag{14}$$

In a next step, we add the two Eqs. (13) and (14), and explore the relation

$$\boldsymbol{n} = \boldsymbol{n}_1 = -\boldsymbol{n}_2 \,; \quad \frac{\partial p_{\mathrm{a}1}}{\partial \boldsymbol{n}_1} = \frac{\partial p_{\mathrm{a}1}}{\partial \boldsymbol{n}} = \frac{\partial p_{\mathrm{a}2}}{\partial \boldsymbol{n}_2} = -\frac{\partial p_{\mathrm{a}2}}{\partial \boldsymbol{n}}$$

to arrive at

$$\int_{\Omega_1} \frac{1}{c^2}\, w_1 \ddot{p}_{\mathrm{a}1} \mathrm{d}\boldsymbol{x} + \int_{\Omega_1} \nabla w_1 \cdot \nabla p_{\mathrm{a}1} \mathrm{d}\boldsymbol{x} + \int_{\Omega_2} \frac{1}{c^2}\, w_2 \ddot{p}_{\mathrm{a}2} \mathrm{d}\boldsymbol{x} + \int_{\Omega_2} \nabla w_2 \cdot \nabla p_{\mathrm{a}2} \mathrm{d}\boldsymbol{x} - \int_{\Gamma_\mathrm{I}} [w] \frac{\partial p_{\mathrm{a}1}}{\partial n}\, \mathrm{d}\boldsymbol{s} = \int_{\Omega_1} w_1 g_1 \, \mathrm{d}\boldsymbol{x} + \int_{\Omega_2} w_2 g_2 \, \mathrm{d}\boldsymbol{x} \,. \tag{15}$$

In (15) the operator [ ] defines the jump operator, e.g., $[w] = w_1 - w_2$. In order to retain symmetry, we add to (15) the following term

$$-\int_{\Gamma_\mathrm{I}} [p_\mathrm{a}] \frac{\partial w_1}{\partial n}\, \mathrm{d}\boldsymbol{s} \quad \text{with} \quad [p_\mathrm{a}] = p_{\mathrm{a}1} - p_{\mathrm{a}2} \,.$$

This operation is allowed, since $[p_\mathrm{a}]$ is forced to be zero at the interface. In a final step, we add along the interface Γ_I the term

$$\beta \sum_E \frac{1}{h_E} \int_{\Gamma_E} [p_\mathrm{a}]\, [w]\, \mathrm{d}\boldsymbol{s} \tag{16}$$

with β the penalty factor. In (16) h_E is a characteristic length scale of each interface element E (space discrete level). Therewith, we arrive at the following final formulation for Nitsche-type mortaring

$$\int_{\Omega_1} \frac{1}{c^2}\, w_1 \ddot{p}_{\mathrm{a}1} \mathrm{d}\boldsymbol{x} + \int_{\Omega_1} \nabla w_1 \cdot \nabla p_{\mathrm{a}1} \mathrm{d}\boldsymbol{x} + \int_{\Omega_2} \frac{1}{c^2}\, w_2 \ddot{p}_{\mathrm{a}2} \mathrm{d}\boldsymbol{x} + \int_{\Omega_2} \nabla w_2 \cdot \nabla p_{\mathrm{a}2} \mathrm{d}\boldsymbol{x} - \underbrace{\int_{\Gamma_\mathrm{I}} [w] \frac{\partial p_{\mathrm{a}1}}{\partial n}\, \mathrm{d}\boldsymbol{s}}_{\textit{Consistency}} - \underbrace{\int_{\Gamma_\mathrm{I}} [p_\mathrm{a}] \frac{\partial w_1}{\partial n}\, \mathrm{d}\boldsymbol{s}}_{\textit{Symmetrization}}$$

$$\underbrace{+\beta \sum_E \frac{1}{h_E} \int_{\Gamma_E} [p_\mathrm{a}]\,[w]\,\mathrm{d}\boldsymbol{s}}_{Penalty/Stabilization} = \int_{\Omega_1} w_1 g_1\,\mathrm{d}\boldsymbol{x} + \int_{\Omega_2} w_2 g_2\,\mathrm{d}\boldsymbol{x}\,. \tag{17}$$

If the penalty parameter β is chosen large enough, the bilinear form is coercive on the discrete space and one derives optimal a priori error estimates in both the energy norm and the L_2 norm for polynomials of arbitrary degree (Hansbo et al. 2003). In a next step, we perform a spatial discretization according to (7), (8) and arrive at

$$\begin{aligned}
&\int_{\Omega_1} \frac{1}{c^2}\, w_1^h\, \ddot{p}_{\mathrm{a}1}^h\,\mathrm{d}\boldsymbol{x} + \int_{\Omega_1} \nabla w_1^h \cdot \nabla p_{\mathrm{a}1}^h\,\mathrm{d}\boldsymbol{x} - \int_{\Gamma_\mathrm{I}} w_1^h \frac{\partial p_{\mathrm{a}1}^h}{\partial \boldsymbol{n}}\,\mathrm{d}\boldsymbol{s} \\
&- \int_{\Gamma_\mathrm{I}} \frac{\partial w_1^h}{\partial \boldsymbol{n}}\, p_{\mathrm{a}1}^h\,\mathrm{d}\boldsymbol{s} + \int_{\Gamma_\mathrm{I}} \frac{\partial w_1^h}{\partial \boldsymbol{n}}\, p_{\mathrm{a}2}^h\,\mathrm{d}\boldsymbol{s} + \beta \sum_{E(\Gamma_\mathrm{I})} \frac{1}{h_E} \int_{\Gamma_\mathrm{I}} w_1^h\, p_{\mathrm{a}1}^h\,\mathrm{d}\boldsymbol{s} \\
&\qquad - \beta \sum_{E(\Gamma_\mathrm{I})} \frac{1}{h_E} \int_{\Gamma_\mathrm{I}} w_1^h\, p_{\mathrm{a}2}^h\,\mathrm{d}\boldsymbol{s} = \int_{\Omega_1} w_1^h g_1\,\mathrm{d}\boldsymbol{x}
\end{aligned} \tag{18}$$

$$\begin{aligned}
&\int_{\Omega_2} \frac{1}{c^2}\, w_2^h\, \ddot{p}_{\mathrm{a}2}^h\,\mathrm{d}\boldsymbol{x} + \int_{\Omega_2} \nabla w_2^h \cdot \nabla p_{\mathrm{a}2}^h\,\mathrm{d}\boldsymbol{x} + \int_{\Gamma_\mathrm{I}} w_2^h \frac{\partial p_{\mathrm{a}1}^h}{\partial \boldsymbol{n}}\,\mathrm{d}\boldsymbol{s} \\
&+ \beta \sum_{E(\Gamma_\mathrm{I})} \frac{1}{h_E} \int_{\Gamma_\mathrm{I}} w_2^h\, p_{\mathrm{a}2}^h\,\mathrm{d}\boldsymbol{s} - \beta \sum_{E(\Gamma_\mathrm{I})} \frac{1}{h_E} \int_{\Gamma_\mathrm{I}} w_2^h\, p_{\mathrm{a}1}^h\,\mathrm{d}\boldsymbol{s} \\
&\qquad = \int_{\Omega_2} w_2^h g_2\,\mathrm{d}\boldsymbol{x}\,.
\end{aligned} \tag{19}$$

In matrix notation, the discrete system of equations reads as

$$\begin{aligned}
&\begin{pmatrix} \boldsymbol{M}_1 & 0 \\ 0 & \boldsymbol{M}_2 \end{pmatrix} \begin{pmatrix} \underline{\ddot{p}}_{\mathrm{a}1} \\ \underline{\ddot{p}}_{\mathrm{a}2} \end{pmatrix} + \begin{pmatrix} \boldsymbol{K}_1 & 0 \\ 0 & \boldsymbol{K}_2 \end{pmatrix} \begin{pmatrix} \underline{p}_{\mathrm{a}1} \\ \underline{p}_{\mathrm{a}2} \end{pmatrix} \\
&\qquad + \begin{pmatrix} \boldsymbol{K}_{\Gamma_{\mathrm{I}1}} & \boldsymbol{K}_{\Gamma_{\mathrm{I}1}\Gamma_{\mathrm{I}2}} \\ \boldsymbol{K}_{\Gamma_{\mathrm{I}2}\Gamma_{\mathrm{I}1}} & \boldsymbol{K}_{\Gamma_{\mathrm{I}2}} \end{pmatrix} \begin{pmatrix} \underline{p}_{\mathrm{a}1} \\ \underline{p}_{\mathrm{a}2} \end{pmatrix} = \begin{pmatrix} \underline{f}_1 \\ \underline{f}_2 \end{pmatrix}.
\end{aligned} \tag{20}$$

Thereby, $\boldsymbol{M}_k$ and $\boldsymbol{K}_k$ are the standard mass and stiffness matrices, respectively. The additional matrices according to the interface compute as follows

$$\begin{aligned}
\boldsymbol{K}_{\Gamma_{\mathrm{I}1}}^{ij} &= -\int_{\Gamma_{\mathrm{I}1}} N_{1i} \frac{\partial N_{1j}}{\partial \boldsymbol{n}}\,\mathrm{d}\boldsymbol{s} - \int_{\Gamma_{\mathrm{I}1}} \frac{\partial N_{1i}}{\partial \boldsymbol{n}}\, N_{1j}\,\mathrm{d}\boldsymbol{s} \\
&\quad + \beta \sum_{E(\Gamma_{\mathrm{I}1})} \frac{1}{h_E} \int_{\Gamma_E} N_{1i} N_{1j}\,\mathrm{d}\boldsymbol{s}
\end{aligned} \tag{21}$$

$$\boldsymbol{K}^{ij}_{\Gamma_{I1}\Gamma_{I2}} = \int_{\Gamma_{I1}} \frac{\partial N_{1i}}{\partial \boldsymbol{n}} N_{2j}\, \mathrm{d}\boldsymbol{s} - \beta \sum_{E(\Gamma_{I1})} \frac{1}{h_E} \int_{\Gamma_E} N_{1i} N_{2j}\, \mathrm{d}\boldsymbol{s}$$

$$= \left(\boldsymbol{K}^{ij}_{\Gamma_{I2}\Gamma_{I1}}\right)^t \tag{22}$$

$$\boldsymbol{K}^{ij}_{\Gamma_{I2}} = \beta \sum_{E(\Gamma_{I2})} \frac{1}{h_E} \int_{\Gamma_E} N_{2i} N_{2j}\, \mathrm{d}\boldsymbol{s} \tag{23}$$

$$\underline{f}^i_1 = \int_{\Omega_1} N_{1i}\, g_1\, \mathrm{d}\boldsymbol{x}\,; \quad \underline{f}^i_2 = \int_{\Omega_2} N_{2i}\, g_2\, \mathrm{d}\boldsymbol{x}\,. \tag{24}$$

Here, we have already substituted Γ_I by Γ_{I1} as well as Γ_{I2}, which are the discretized interfaces of Ω_1 and Ω_2. Furthermore, the computation of the matrices in (21) and (22) involves basis functions N_1 and N_2, which are defined on different grids. Therefore, grid intersection operations as for the classical Mortar formulation are necessary, see Sect. 4. In addition, we note that Nitsche-type mortaring is equivalent to an IP-DG (Internal Penalty - Discontinuous Galerkin) ansatz along the non-conforming interface Γ_I. Finally, we want to emphasis that both approaches, classical Mortar and Nitsche-type mortaring, are powerful methods to correctly handle non-conforming grids both from a physical and mathematical point of view.

3 Time Discretization

In a final step to arrive at the full discrete system of equations, we have to perform a time discretization. Spurious waves, which are not resolved by the discretization (both in space and time), deteriorate the numerical solution and should be numerically damped. Since numerical damping cannot be introduced in the classical Newmark method without degrading the order of accuracy, we advise to apply a time-stepping scheme with controlled numerical dispersion such as the HHT (Hilber–Hughes–Taylor) method. Thereby, three parameters define the behavior of the time-stepping scheme: α_{HHT}, β_{HHT} and γ_{HHT}. Figure 5 demonstrates the damping behavior of different schemes. As can be seen, the standard trapezoidal scheme introduces no numerical damping. The Newmark scheme, which is just second order accurate for the parameters $\beta_{\mathrm{NM}} = 0.25$ and $\gamma_{\mathrm{NM}} = 0.5$, is able to achieve appropriate numerical damping by degrading to first order accuracy. The HHT method is unconditional stable and 2nd order accurate for $\alpha_{\mathrm{HHT}} \in [-0.3,\ 0]$ and according to the choice of this parameter introduces numerical damping. The two other parameters compute as

$$\beta_{\mathrm{HHT}} = \frac{(1-\alpha_{\mathrm{HHT}})^2}{4}\,; \quad \gamma_{\mathrm{HHT}} = \frac{(1-2\alpha_{\mathrm{HHT}})}{2}\,.$$

For a detailed analysis, we refer to Hughes (2000).

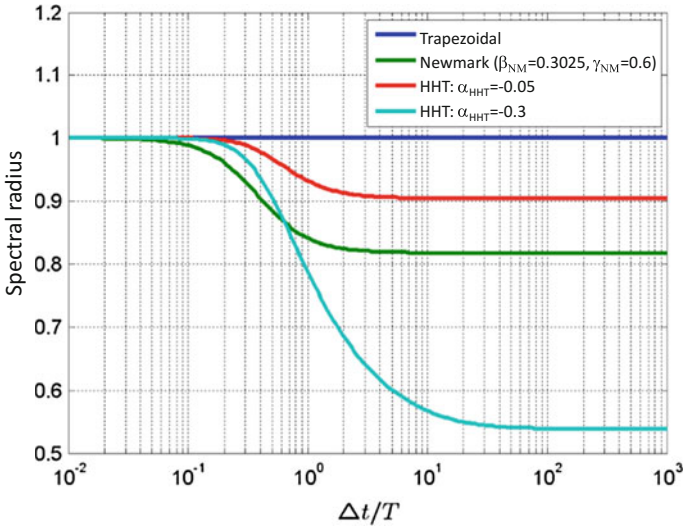

Fig. 5 Spectral radius (defined by the largest eigenvalue of the amplification matrix) over the ratio of time step size Δt to time period T

4 Mesh Intersection Operations

The feature which makes the Mortar and Nitsche-type mortaring so flexible, namely the usage of non-conforming meshes in different sub-domains, comes at the cost of a more elaborate implementation. Since the grids are allowed to be non-conforming on the interfaces of two sub-domains, the integrals defined on these interfaces involving basis functions from both sides have to be evaluated with respect to two different meshes. The decomposition of the global domain is done in a geometrically conforming way however. This guarantees that any interface inherits the discretizations of its neighboring sub-domains. It is necessary to compute the domains, where pairs of elements on the interface intersect. The corresponding integrals are then evaluated over these domains of intersection and it is up to the assembly operator to assemble the corresponding results into the correct positions of the coupling matrices.

In the following we denote the interface between two sub-domains Ω_j and Ω_k by Γ_{jk}. The triangulations corresponding to Ω_j and Ω_k are labeled $\mathcal{T}_j$ and $\mathcal{T}_k$. The nodal basis functions on $\mathcal{T}_j$ shall be denoted by N_{ja} and the ones defined on $\mathcal{T}_k$ are N_{kb}. An integral over the interface may then be written in terms of the basis function as

$$\int_{\Gamma_{jk}} N_{ja}\, N_{kb}\, \mathrm{d}\boldsymbol{s}. \tag{25}$$

For numerically evaluating this integral, we first have to determine the subsets of the interface, where pairs of elements intersect. In 2D the interfaces between sub-

domains are curves. Therefore, we have to consider the intersection of line elements in this case. If the interface is planar these are simple interval checks. If the interface is curved, we first have to project the elements onto a common line segment and do the interval checks there. These considerations also apply in a modified way for domains in 3D, where interfaces are surfaces. We have to note however that the seemingly simple operation of finding the intersection domain of arbitrary surface elements is a highly non-trivial task even for first order elements with straight edges. The last named case is however closely related to a problem in computer graphics. There 2D polygons generated during the rendering of 3D scenes have to be clipped against a view-port (cf. Greiner and Hormann 1998). Strategies and algorithms for dealing with the mesh intersection problem have been sought after for a long time in the area of domain decomposition. A small selection of available methods can be found in Puso and Laursen (2002), Park and Felippa (2002), Heinstein and Laursen (2003), Puso (2004).

If no neighborhood information between the elements on the interfaces is available and if a naive approach is taken, the operation of finding the intersection domains of all pairs of elements is of complexity $O(m \cdot n)$. Here m is the number of elements on the master side and n is the number of elements on the slave side. The operation is so expensive, since every element on the slave side has to be checked for intersection with every element on the master side and no assumptions about neighborhood are being made.

By applying space partitioning algorithms the required effort for this operation may however be drastically reduced. If neighborhood information is present in addition, an advancing front algorithm may be applied which is described in Gander and Japhet (2009). It starts at a known pair of intersecting elements and then proceeds with the intersection checks at the neighboring elements. The algorithm therewith achieves linear complexity. This improvement is of crucial importance when dealing with applications, like rotating domains (Kaltenbacher et al. 2016a), where the intersection domains have to be recomputed after each time step.

The final step is to compute the value of the integrals on the intersection domains. The method we describe here has shown to be robust and can be implemented also in FE codes, which do not provide analytical parameterizations of the domain geometry.

4.1 Intersection of Two Line Elements

If an intersection of two co-linear line elements exists, it is again a line element sharing two of the four endpoints of both parent elements in the co-linear case. To check for an intersection one has to project the endpoints $[\mathbf{m}_1, \mathbf{m}_2]$ in two dimensional coordinates of the element on the master side of the interface to the one dimensional local coordinate system defined by the endpoints of the slave element $[\mathbf{s}_1, \mathbf{s}_2]$.

The local coordinates of the slave nodes $[\mathbf{s}_1, \mathbf{s}_2]$ are trivially given by 0 and 1. The four local coordinates of the pair of lines are then brought into ascending order

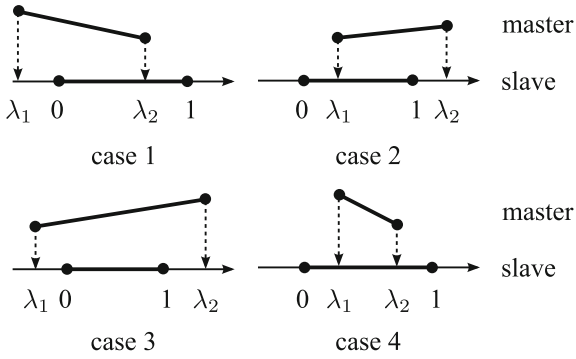

Fig. 6 Four possible cases of two lines intersecting each other

and therefore four possible cases for the intersection of two line elements may be identified as depicted in Fig. 6:

1. $\lambda_1 \leq 1 \ \wedge \ 0 < \lambda_2 < 1$: the intersection is the line $[\mathbf{s}_1, \mathbf{m}_2]$
2. $0 < \lambda_1 < 1 \ \wedge \ \lambda_2 \geq 1$: the intersection is the line $[\mathbf{m}_1, \mathbf{s}_2]$
3. $\lambda_1 \leq 0 \ \wedge \ \lambda_2 \geq 1$: the intersection is the line $[\mathbf{s}_1, \mathbf{s}_2]$
4. $\lambda_1 > 0 \ \wedge \ \lambda_2 < 1$: the intersection is the line $[\mathbf{m}_1, \mathbf{m}_2]$

We note that new points have to be generated at the projection positions on the slave element for curved interfaces in the cases 1, 2 and 4.

4.2 Intersection of Two Axis-Parallel Quadrilateral Elements

The algorithm for finding intersections of lines can be extended in a straight forward manner to a 3D setting if only axis-parallel quadrilateral elements are present on the interface. The term axis-parallel does not refer to the global coordinate axes in this context, but to the fact that the quadrilateral edges on both sides of the interface have to be parallel. This includes the case of parallelogram-shaped quadrilaterals as depicted in Fig. 7. We again compute the local coordinates (λ_1, μ_1) and (λ_2, μ_2) of the first and third corner of the master element in respect to the slave element. After bringing the local coordinates for both directions into ascending order there are sixteen possible cases for the intersection of two quadrilaterals. The ordering is necessary due to the fact that the order of nodes for elements is just guaranteed to be counter-clockwise, but the master element might have been rotated in respect to the slave element as a whole. In addition, we have to mention however that there exist many more possibilities of intersection for pairs of triangles, pairs of triangles and quadrilaterals or pairs of arbitrary shaped quadrilaterals than for the simple configuration given here. These situations require a more sophisticated treatment. A description of the algorithm used to treat arbitrary element types on curved interfaces can be found in Grabinger (2007).

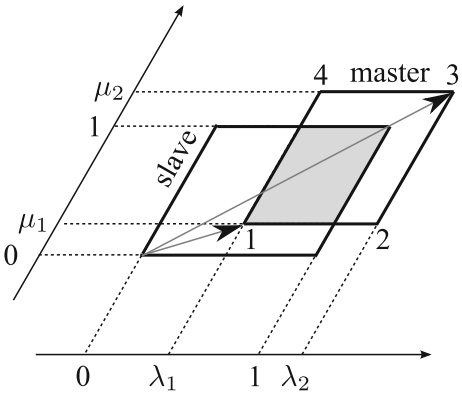

Fig. 7 Intersection of two axis-parallel parallelogram-shaped elements

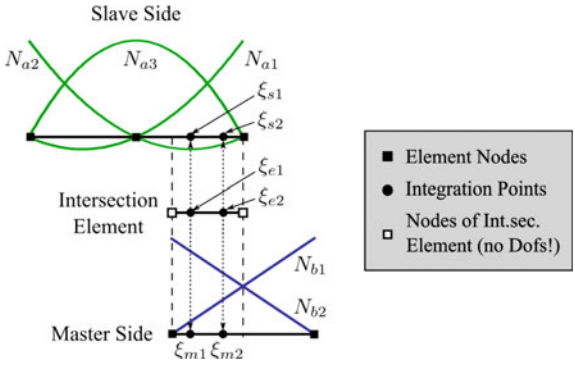

Fig. 8 Projection of quadrature points from the intersection element into the master element which is of first order and into the slave element which is of second order in this example

4.3 Evaluation of the Coupling Integrals

Once the intersection elements have been found, the coupling integral (25) can be evaluated on these elements by means of standard Gauss quadrature

$$\int_{\Gamma_{jk}} N_{ja}\, N_{kb}\, \mathrm{d}\boldsymbol{s} = \sum_{e=1}^{n_{\text{isec}}} \int_{\Gamma_e} N_a\, N_b\, \mathrm{d}\boldsymbol{s} \approx$$

$$\approx \sum_{e=1}^{n_{\text{isec}}} \sum_{l=1}^{n_{\text{int}}} W_l N_a(\boldsymbol{\xi}_l^m) N_b(\boldsymbol{\xi}_l^s) \mathcal{J}^e(\boldsymbol{\xi}_l^e)\ . \tag{26}$$

Here n_{isec} is the number of intersection elements, n_{int} is the number of quadrature points, W_l are the quadrature weights and the determinant of the Jacobian $\mathcal{J}^e$ accounts for the element mapping. The difficulty which arises when this quadrature formula is applied, is that only the quadrature point $\boldsymbol{\xi}_l^e$ in respect to the local coordinates of the intersection element is known in advance and that the points $\boldsymbol{\xi}_l^m$ in the master element and $\boldsymbol{\xi}_l^s$ in the slave element have to be projected into those elements, before the basis functions can be evaluated there (see Fig. 8). It is very important to notice that nodes

of the intersection element do not carry any degrees of freedom by themselves. The intersection element is just an auxiliary geometrical entity, which only serves as integration domain. The projection operation for general elements involves the following steps:

1. Map local coordinates $\boldsymbol{\xi}_l^e$ of quadrature point in intersection element to global coordinates
2. Map global coordinates of quadrature point to local coordinates $\boldsymbol{\xi}_l^m$ of master element
3. Map global coordinates of quadrature point to local coordinates $\boldsymbol{\xi}_l^s$ of slave element

Points 2 and 3 in general involve the application of a Newton–Raphson algorithm. A linear mapping algorithm may only be used for 2-node isoparametric line elements, 3-node isoparametric triangle elements or higher order elements which just use a linear local-to-global mapping. Once the values of the basis functions N_a and N_b have been obtained and (26) has been evaluated, the assembly operator has to make sure, that the contribution gets added to the corresponding entry in the coupling matrix.

5 Application to Aeroacoustics

5.1 Cylinder in Cross Flow

As a first practical application, the generation of sound due to a cylinder mounted on a plate in cross-flow is investigated. This simple geometry is nonetheless interesting to analyze since variations of it are very common sources for flow induced noise (e.g. antennas on cars, flagpoles, etc.). Understanding the mechanisms of sound generation for this geometry may therefore give important hints to engineers on how to reduce noise levels for similar settings. The described setting has already been subject to closer empirical and numerical investigations (c.f. Escobar 2007; Hahn 2008).

For the cylinder with rectangular cross-section having a side-length D of 20 mm (see Fig. 9), the first occurring main frequency is in the range from 50 to 60 Hz at a mean flow velocity of 10 m/s. Given the speed of sound in air at standard conditions ($c = 343$ m/s) results in a wavelength λ of about 5.72 m. Resolving the wavelength by 20 finite elements with basis functions of 1st order results in an edge length of the finite elements, which corresponds to the dimensions of the domain, on which the flow is computed. This fact alone motivates the usage of non-conforming grids at the interface towards the acoustic propagation domain.

CFD The domain, on which the flow is computed and which corresponds to the acoustic source domain, is displayed in Fig. 9. Thereby, the research program FASTEST-3D (Durst and Schäfer 1996) and the commercial software ANSYS-CFX are applied for the flow computation. The boundary conditions used in the fluid

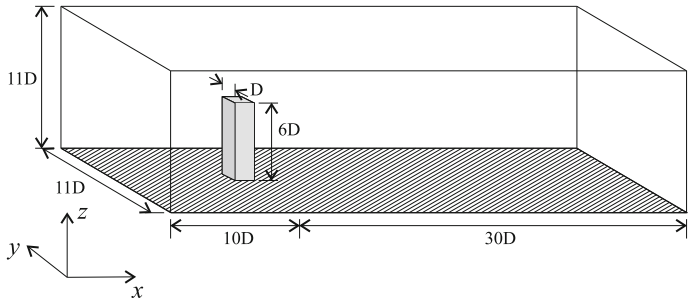

Fig. 9 Numerical domain used for fluid computations depicting dimensions. D = 20 mm

Table 1 Boundary conditions used for fluid computations

Position	Boundary condition
X = 0	Inlet profile based on experiments
X = 40D	Convective exit boundary
Z = 11D	Symmetry boundary condition
Y = 0, Y = 11D	Symmetry boundary condition
Cylinder surface and bottom	No slip boundary condition

computation with respect to the configuration from Fig. 9 are described in Table 1. Therewith, we have used a measured inflow profile with a mean velocity of 10 m/s resulting in a Reynolds number of about 13.000. FASTEST-3D uses a LES (Large Eddy Simulation) turbulence model to accurately resolve the flow structure. After a grid study, the computations have been performed on a grid with 3.1 million cells having strong refinements at the critical regions close to the cylinder and the wall. The nearest grid point in dimensionless wall coordinates is at $y^+ = 2$. The time step size was set to $\Delta t_\mathrm{f}^{LES} = 10\,\mu\mathrm{s}$, which guaranteed a resolution of up to 10 kHz, and which resulted in a CFL-number of 2.1.

For the simulation of the flow using the code ANSYS-CFX, a turbulence modeling approach based on SAS (Scale Adaptive Simulation) was employed (Menter and Egorov 2005). The SAS approach allowed us to coarsen the grid of the LES computations to about 1.1 million, which resulted in a shorter computational time and less memory usage. Regarding the time discretization, a time step size of $\Delta t_\mathrm{f}^{SAS} = 2\Delta t_\mathrm{f}^{LES} = 20\,\mu\mathrm{s}$ was used.

To get an impression about the flow field, we show in Fig. 10 the flow structure as obtained by ANSYS-CFX for a characteristic time step. The displayed results are iso-surfaces of $\boldsymbol{\omega}^2 - \boldsymbol{\epsilon}^2 = 100{,}000\,\mathrm{s}^{-2}$ colored with the eddy viscosity (here $\boldsymbol{\omega}$ representing the vorticity and $\boldsymbol{\epsilon}$ the strain rate). One can clearly see the horseshoe, the roof and span-wise vortex structure. In studying animations of the flow structure, one can observe a strong interaction between the roof and span-wise vortex, which results in a reduced vortex street behind the cylinder. For a quantitative comparison

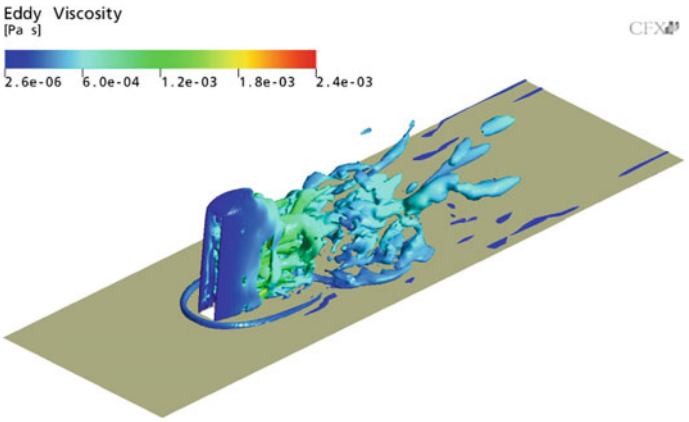

Fig. 10 Instantaneous visualization of transient flow field using SAS turbulence modeling

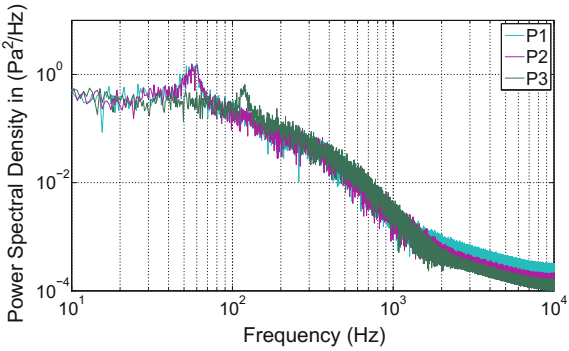

Fig. 11 Frequency spectra of the wall pressure fluctuation at different monitor points obtained by LES

between LES and SAS computations we show in Figs. 11 and 12 the spectra of the wall pressure fluctuations at different monitor points as listed in Table 2. In both simulations, pressure fluctuations on the side walls (monitoring points P1 and P2) of the cylinder show the characteristic vortex shedding frequency of about 55 Hz, which are in good agreement with experiments (Becker et al. 2008). In addition, the pressure fluctuations at monitoring point P3, which is located on the bottom behind the cylinder, exhibit in both simulations a dominant frequency at twice the vortex shedding frequency. At this point it should be noted that for both LES- and SAS-based data no significant differences were found in the acoustic field.

Acoustics The computational domain for acoustics, as it is depicted in Fig. 13, consists of the source domain, a propagation domain and a Perfectly Matched Layer (PML) to account for free field radiation (Kaltenbacher 2015). On the bottom plane as well as on the faces of the cylinder sound-hard walls are modeled by applying homogeneous Neumann boundary conditions. Here, we solve the inhomogeneous wave equation of Lighthill in the frequency domain

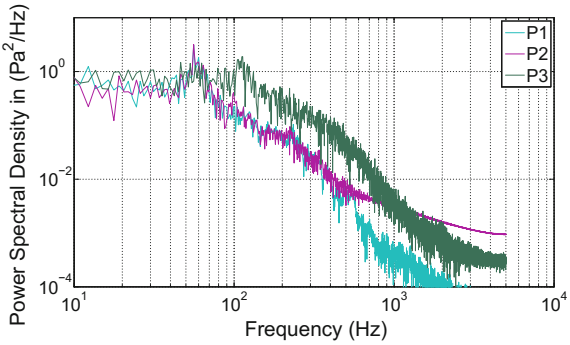

Fig. 12 Frequency spectra of the wall pressure fluctuation at different monitor points obtained by SAS

Table 2 Points at which we have evaluated the wall pressure spectra (see Fig. 9)

Position	P01	P02	P03
X	10.5 D	10.5 D	15.0 D
Y	5.0 D	6.0 D	5.5 D
Z	3.0 D	3.0 D	0.0 D

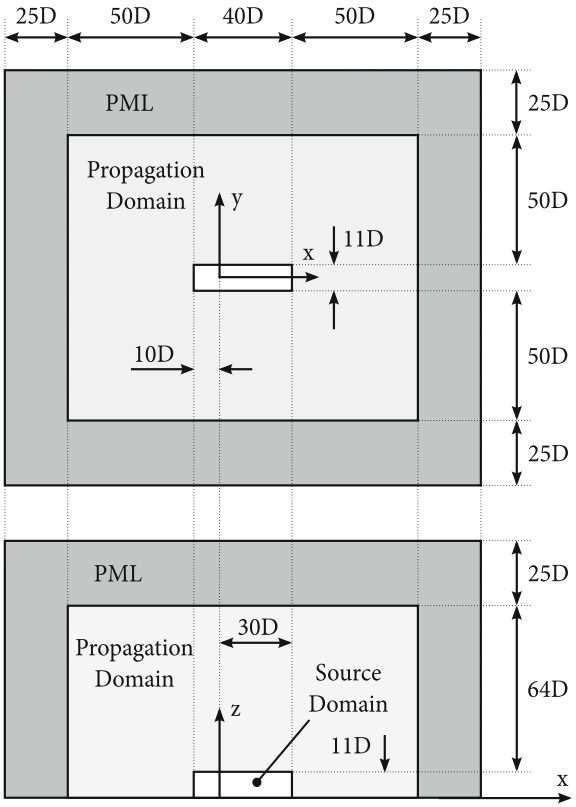

Fig. 13 Geometry of acoustic domain for harmonic simulation

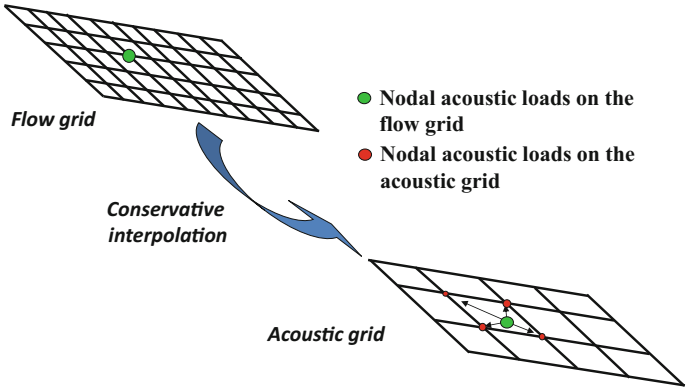

Fig. 14 Conservative interpolation from a fine CFD grid to a coarser acoustic grid

$$\frac{\partial^2 \hat{p}'}{\partial x_i^2} + k^2 \hat{p}' = -\frac{\partial^2 \hat{T}_{ij}}{\partial x_i \partial x_j} \tag{27}$$

with the harmonic pressure fluctuation $\hat{p}'$, the wavenumber k and the Fourier transformed entries $\hat{T}_{ij}$ of Lighthill's tensor. Due to the low Mach number, we approximate the entries $T_{ij}(t)$ by

$$T_{ij}(t) \approx \rho_0 v_i(t) v_j(t) \tag{28}$$

with the mean density ρ_0 and flow velocity $\boldsymbol{v}$. Here, we apply the proposed Mortar formulation, which allows to combine different meshes for the source and propagation domains and flexibly build up a global mesh specially suited for the aeolian tones which are expected in the analysis.

A crucial point for each hybrid aeroacoustic approach is the transformation of the acoustic sources from the flow grid to the acoustic grid. In order to preserve the acoustic energy, we perform an integration over the source volume (corresponding to the computational flow region) within the FE formulation and project the results to the nodes of the fine flow grid, which has to be interpolated to the coarser acoustic grid (see Fig. 14). Thereby, our interpolation has to be conservative in order to preserve the total acoustic energy. As illustrated in Fig. 14, we have to find for each nodal source F_k^{f} of the flow grid in which finite element of the acoustic grid it is located. Then, we compute from the global position $\boldsymbol{x}_k$ its local position $\boldsymbol{\xi}_k$ in the reference element. This is in the general case a nonlinear mapping and is solved by a Newton scheme. Now, with these data we can perform a bilinear interpolation and add the contribution of F_k^{f} to the nodes of the acoustic grid by using the standard finite element basis functions N_i (Kaltenbacher et al. 2010)

$$F_i^{\mathrm{a}} = F_i^{\mathrm{a}} + N_i(\boldsymbol{\xi}_k) F_k^{\mathrm{f}}. \tag{29}$$

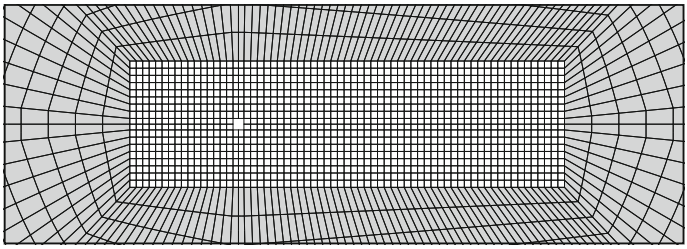

Fig. 15 Details of the conforming mesh. A 2D cut in the xy-plane is depicted

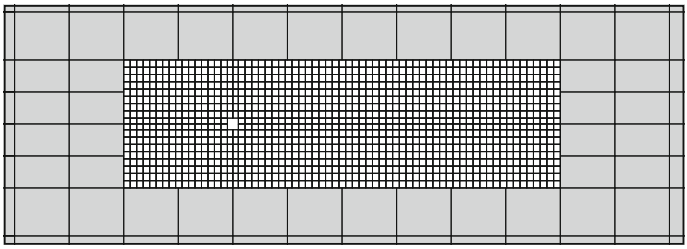

Fig. 16 Details of the non-conforming mesh. A 2D cut in the xy-plane is depicted

In order to demonstrate the capability of the non-conforming grid technique, a few test cases are defined. Cuts of the reference mesh and our non-conforming mesh are depicted in the vicinity of the source domain Ω_{a1} in Figs. 15 and 16. Thereby, the following different grids and order of FE basis functions have been investigated:

- **SQCONF**: A conforming mesh consisting of 20-node hexahedra is used, see Fig. 15. The results in Kaltenbacher et al. (2010) have been obtained with this mesh.
- **SQQUQU**: The same mesh as in the SQCONF case is used in Ω_{a1} (source domain) but a Cartesian 20-node hexahedra mesh is used in the propagation domain Ω_{a2} (cf. Fig. 16). The mesh in Ω_{a2} has a very fine discretization, namely, about 120 degrees of freedom per wavelength at 55 Hz.
- **SQLIQU**: For this case linear elements (8-node) of the mesh in Ω_{a1} are used, which contain the same corner nodal sources as the one in SQCONF. This reduces the number of unknowns in the source region by a factor of four compared to the quadratic mesh. The same 20-node hexahedra mesh as in SQQUQU is used in the propagation domain.
- **SQLILI**: In order to substantially decrease the number of unknowns also in the propagation region Ω_{a2} trilinear hexahedron elements are used in that domain. In comparison to the SQLIQU case, the topology of the mesh in Ω_{a2} stays the same. This cuts down the number of unknowns to one fourth also in the propagation domain. One can expect little or no impact on the accuracy of the solution, since the mesh still has a resolution of about 60 degrees of freedom per wavelength at

Table 3 Number of unknowns and wall clock times for the square cylinder cases

Test case	Ω_{a1}	Ω_{a2}	Total	Wall clock time (s)
SQCONF	93,781	444,652	538,433	1404.0
SQQUQU	93,781	142,163	236,437	202.0
SQLIQU	24,177	142,163	166,833	131.0
SQLILI	24,177	36,386	60,738	26.0

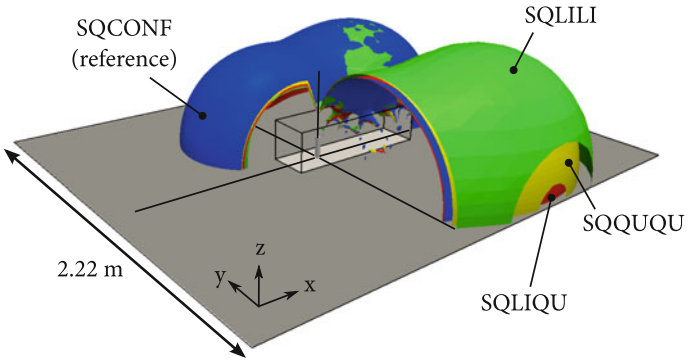

Fig. 17 Square cylinder with isosurfaces of acoustic pressure ($p_a = 6$ mPa)

55 Hz. Compared to the reference setup, the number of unknowns is reduced by a factor of nine.

Table 3 gives an overview of the number of unknowns for the acoustic computations. The solver and the number of threads on the used computer hardware are kept the same. The times clearly correspond to the total number of unknowns for each case. The results show that the computation in the SQLILI case is 54 times faster than in the reference case while still yielding comparable results. In all non-conforming cases, the Lagrange multiplier is defined on the coarse discretization of the surface Γ_I. In all simulations Ω_{a2} is used as the slave side and Ω_{a1} is used as the master.

The results of the computations for the vortex shedding frequency at 55 Hz are shown in Fig. 17 as isosurfaces of the acoustic pressure field and in Figs. 18, 19 and 20 as directivity plots in the xy-plane. It is obvious that all four configurations produce almost the same results.

5.2 Axial Fan

The cabin noise of modern ground vehicles is highly affected by flow related noise sources. This is especially the case, when the vehicle is not moving. Thereby, fan and outlet of air-conditioning systems are main acoustic sources and may reduce the

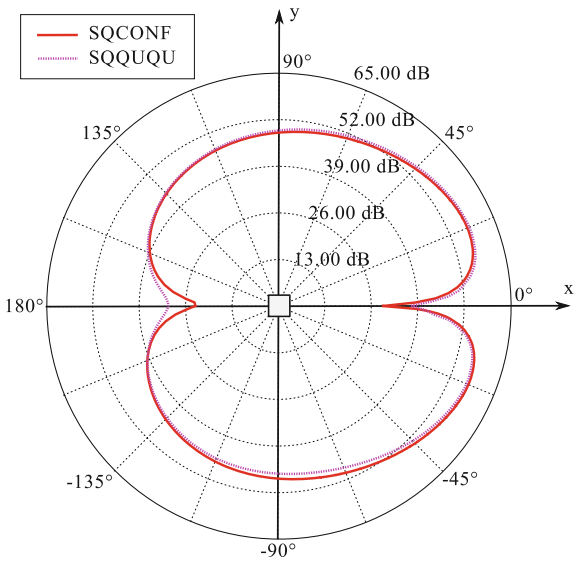

Fig. 18 Directivity plots of sound pressure levels at z = 0 in 1 m distance of the square cylinder for SQQUQU

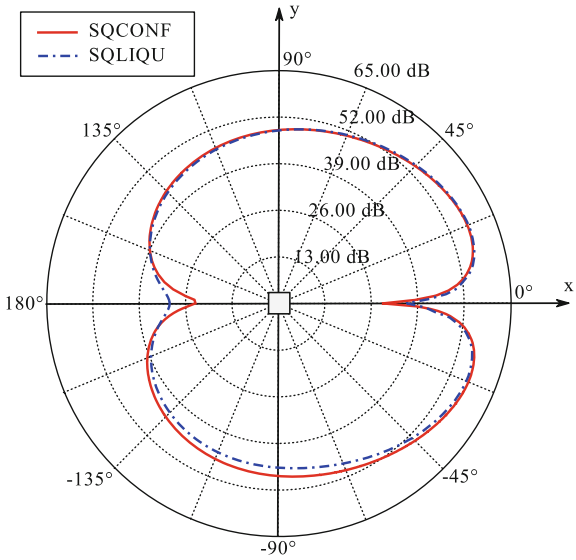

Fig. 19 Directivity plots of sound pressure levels at z = 0 in 1 m distance of the square cylinder for SQLIQU

comfort significantly. Rotating fans generate a highly turbulent flow field and can be identified as the main noise source in air conditioning units. Therefore, we focus on flow simulations of rotating fans in air conditioning units using the Arbitrary Mesh Interface (AMI) as implemented in OpenFOAM. For the computation of the acoustic sources, highly accurate unsteady CFD simulation data is needed. Therefore, the transient simulations are carried out by using a DES (Detached Eddy Simulation) turbulence model to accurately resolve the complex flow field. In addition, acoustic

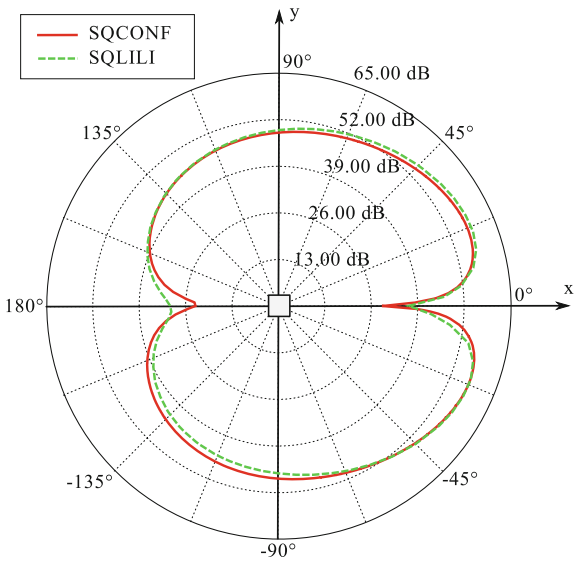

Fig. 20 Directivity plots of sound pressure levels at z = 0 in 1 m distance of the square cylinder for SQLILI

simulations applying the proposed Nitsche-type mortaring to couple the acoustic field between rotating and stationary sub-domains are performed.

Aeroacoustic Formulation The acoustic/viscous splitting technique for the prediction of flow induced sound was first introduced by Hardin and Pope (1994), and afterwards many groups presented alternative and improved formulations for linear and non linear wave propagation (Shen and Sørensen 1999; Ewert and Schröder 2003; Seo and Moon 2005; Munz et al. 2007). These formulations are all based on the idea, that the flow field quantities are split into compressible and incompressible parts. We apply a generic splitting of physical quantities to the Navier–Stokes equations. For this purpose we choose the following ansatz (Hüppe 2013)

$$p = \bar{p} + p_{\mathrm{ic}} + p_{\mathrm{c}} = \bar{p} + p_{\mathrm{ic}} + p_{\mathrm{a}} \tag{30}$$

$$\boldsymbol{v} = \bar{\boldsymbol{v}} + \boldsymbol{v}_{\mathrm{ic}} + \boldsymbol{v}_{\mathrm{c}} = \bar{\boldsymbol{v}} + \boldsymbol{v}_{\mathrm{ic}} + \boldsymbol{v}_{\mathrm{a}} \tag{31}$$

$$\rho = \bar{\rho} + \rho_{\mathrm{l}} + \rho_{\mathrm{a}}\,. \tag{32}$$

Thereby the field variables are split into mean ($\bar{p}$, $\bar{\boldsymbol{v}}$, $\bar{\rho}$) and fluctuating parts just like in the Linearized Euler Equations (LEE). In addition the fluctuating field variables are split into acoustic (p_{a}, $\boldsymbol{v}_{\mathrm{a}}$, ρ_{a}) and flow components (p_{ic}, $\boldsymbol{v}_{\mathrm{ic}}$). Finally, a density correction ρ_{l} is build in according to (32). This choice is motivated by the following assumptions:

- The acoustic field is a fluctuating field.
- The acoustic field is irrotational, i.e. $\nabla \times \boldsymbol{v}_{\mathrm{a}} = 0$, and therefore may be expressed by the acoustic scalar potential ψ_{a} via

$$\boldsymbol{v}_\mathrm{a} = -\nabla\psi_\mathrm{a}\,. \tag{33}$$

- The acoustic field requires compressible media and an incompressible pressure fluctuation is not equivalent to an acoustic pressure fluctuation.

By doing so, we arrive for an incompressible flow at the following perturbed convective wave equation (PCWE) (Kaltenbacher et al. 2016b)

$$\frac{1}{c^2}\,\frac{D^2\psi_\mathrm{a}}{Dt^2} - \Delta\psi_\mathrm{a} = -\frac{1}{c^2\bar{\rho}}\,\frac{Dp_\mathrm{ic}}{Dt}\,;\quad \frac{D}{Dt} = \frac{\partial}{\partial t} + \overline{\boldsymbol{v}}\cdot\nabla\,. \tag{34}$$

Now, as shown in Donea et al. (2004), we may apply an ALE (Arbitrary Lagrangian Eulerian) formulation to couple rotating and stationary domains. Thereby, our operator D/Dt changes to

$$\frac{D}{Dt} \rightarrow \frac{\tilde{D}}{\tilde{D}t} = \frac{\partial}{\partial t} + (\overline{\boldsymbol{v}} - \boldsymbol{v}_\mathrm{r})\cdot\nabla \tag{35}$$

with $\boldsymbol{v}_\mathrm{r}$ the mechanical velocity of rotating parts. Finally, the acoustic pressure p_a computes by

$$p_\mathrm{a} = \bar{\rho}\frac{\tilde{D}\psi_\mathrm{a}}{Dt}\,. \tag{36}$$

Thereby, PCWE is an exact reformulation of the acoustic perturbation equations (APE) (Ewert and Schröder 2003). This convective wave equation fully describes acoustic sources generated by incompressible flow structures and its wave propagation through flowing media. In addition, instead of the original unknowns acoustic pressure p_a and acoustic particle velocity $\boldsymbol{v}_\mathrm{a}$, this formulation has just the scalar unknown ψ_a, which strongly reduces computational time.

5.3 Numerical Computations

We investigate the aeroacoustic field of an axial fan in a duct as displayed in Fig. 21. The fan is embedded in a sound hard tube. The inlet and outlet openings on each side lead into a non reverberant chamber to emulate free field sound propagation. The rotational speed of the fan is about 1500 rpm, which results in a tip speed of the blades of 38.89 m/s. We use the OpenFOAM (Open Field Operation and Manipulation) CFD Toolbox version 2.3.0 for performing the flow computations. Since version 2.1.0 the arbitrary mesh interface (AMI) was implemented based on the algorithm described in Farrell and Maddison (2011). The AMI allows simulation across disconnected, but adjacent mesh domains, which are especially required for rotating geometries.

The flow solution is computed using an adapted version of the pimpleDyMFoam solver implemented in OpenFOAM, which can handle dynamic meshes with a time

Fig. 21 Axial fan

step size of $\Delta t = 10\,\mu$s. For the CFD computation a hex-dominant finite volume mesh consisting of 29.8 million cells was created by using the automatic mesh generator HEXPRESS^{TM}/Hybrid from Numeca. The transient simulation was carried out by using a detached-eddy simulation based on the Spalart–Allmaras turbulence model to accurately resolve the complex flow field (Spalart and Allmaras 1994). The calculation was performed on the Vienna Scientific Cluster VSC2 with 256 cores. Figure 22 displays the velocity field for a characteristic time step. Based on the computed instationary flow pressure, we display the surface contours of the acoustic sources (substantial derivative of the incompressible flow pressure, see (34)) in Fig. 23 for a characteristic time step. In accordance to the flow computation, the rotating domain is embedded into a quiescent propagation region (see Fig. 24). Furthermore, we add at the inflow and outflow boundaries of the CFD domain two additional regions, on which we apply an advanced *Perfectly-Matched-Layer* technique to effectively approximate acoustic free field conditions (Kaltenbacher et al. 2013). Figure 25 displays the computed power spectral density of the acoustic pressure and compares it to the measured one. Thereby, we display the smoothed measured spectra obtained from the 30 s recorded pressure signals as well as the individual spectra by just using measured data of 0.1 s (in gray). The spectra based on our numerical simulation is computed out of a real time simulation of 0.06 s.

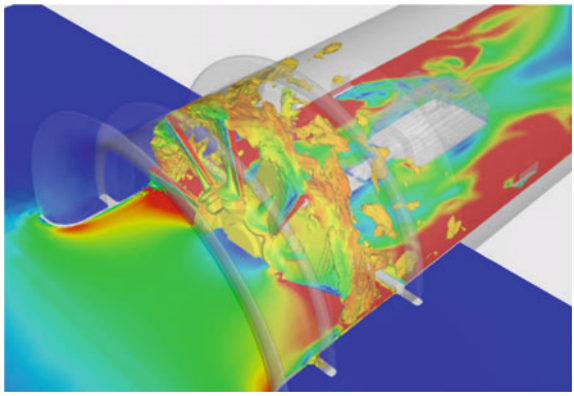

Fig. 22 Flow structure of a characteristic time step

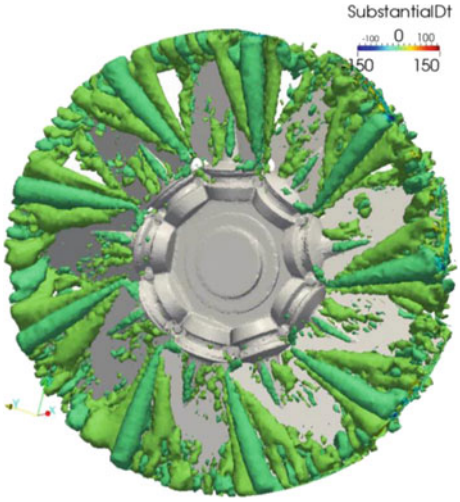

Fig. 23 Visualization of the acoustic source terms at a characteristic time step

5.4 Human Phonation

The voice production mechanisms have been investigated both by means of measurements (on physical replicas, excised animal or human larynges or in living subjects) and numerical simulations. The experimental investigation, especially in vivo, brings numerous complications. Since the advent of affordable high-performance computing, the computer simulation methods based on modeling the fundamental physical phenomena using partial differential equations and solving them numerically have been steadily gaining importance.

An extensive review of numerical models of human phonation can be found in Alipour et al. (2011). The vibration of the real human vocal folds is flow-induced. However, the fully coupled fluid-structure simulations, e.g., Link et al. (2009), Seo and Mittal (2011) always suffer from a lack of accurate geometrical and material

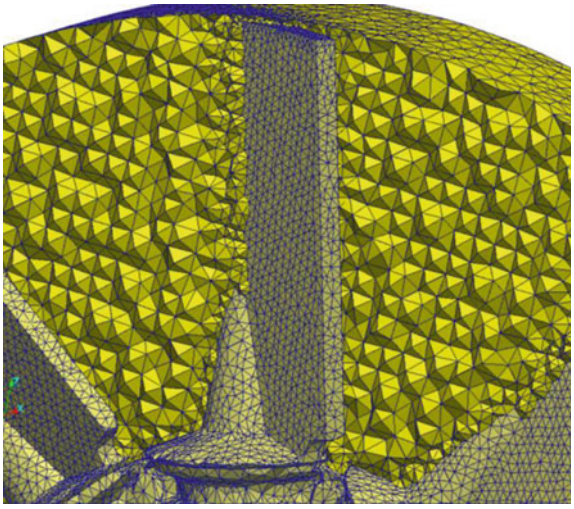

Fig. 24 Detail of the computational CFD grid

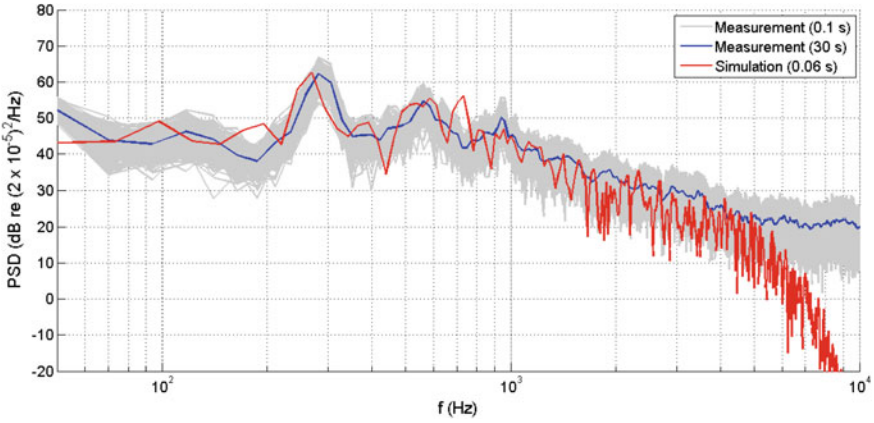

Fig. 25 Power spectral density of the acoustic pressure at measurement position

properties of the living tissues. This is due to the fact that the parameters are highly subject-specific, and also because most of the vocal fold tissue measurements, e.g., Zörner et al. (2010), Kelleher et al. (2013), are still hardly applicable in vivo to precisely determine the vocal fold material parameters. As shown by Zörner et al. (2013), the full fluid-structure interaction solution can be approximated by prescribed vocal fold motion, provided that the boundary conditions are set properly. In this case, it is crucial that the vocal fold vibration patterns mimic the motion of the real human vocal folds sufficiently well. The kinematic parameters have been intensively studied by videokymographic (Svec and Schutte 2012) and high-speed imaging methods (Döllinger et al. 2011), and the results of the experimental studies will be used in our model.

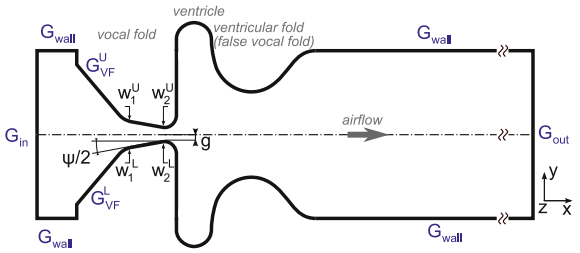

Fig. 26 Geometric model of the human larynx in coronal section. The length of the supra-glottal channel is not to scale

Table 4 Parameters of the kinematic model: Superscripts L and U refer to the lower and upper vocal fold, respectively, $D = 12\,\text{mm}$ is the anterior-posterior length of the vocal folds

$A_1{}^U$, $A_2{}^U$	$A_1{}^L$, $A_2{}^L$	ξ	$m(z)$
0.3 mm	0.3 mm	$\pi/2$	$\sin(\pi z/D)$

$\psi^U/2$	$\psi^L/2$	$g_{\max}$	$g_{\min}$
$-12° \ldots 12°$	$-12° \ldots 12°$	0.72 mm	0.2 mm

Geometry and vocal fold kinematics The flow field is solved on a simplified model of larynx, consisting of a short straight sub-glottal region, the vocal folds, ventricles and false vocal folds (FVFs), and a supra-glottal region (see Fig. 26). In the straight sub-glottal and supra-glottal segments, the model has a square cross-section of $12 \times 12\,\text{mm}$, with vocal and ventricular folds having a length of 7.2 and 6.3 mm, respectively. The detailed dimensions of the flow domain can be found in Šidlof et al. (2014). During the CFD simulation the vocal folds, forming part of the channel boundary, oscillate. The kinematics of the vocal folds were programmed to allow for two-degree-of-freedom, convergent-divergent motion of each of the vocal folds, with prescribed sinusoidal displacement of the inferior and superior vocal fold margins in the medial-lateral direction

$$\begin{aligned} w_1(z,t) &= w_{10} + A_1\,(1 - m(z)) + m(z) A_1 \sin(2\pi f t + \xi) \\ w_2(z,t) &= w_{20} + A_2\,(1 - m(z)) + m(z) A_2 \sin(2\pi f t)\,. \end{aligned} \tag{37}$$

In (37) f is the frequency of vibration, ξ the phase difference between the inferior and superior margin, $A_{1/2}$ the amplitudes and $m(z)$ the anterior-posterior modulation function determining the glottal opening shape (see also Fig. 26 and Table 4). The coordinates in (37) determine uniquely the glottal half-gap g and the medial surface convergence angle ψ.

Flow model and boundary conditions In regular human phonation the air flows at low Mach numbers ($\text{Ma} < 0.2$) and can thereby be regarded as incompressible. This sets the fluid density ρ to a constant value and results in the 3D time dependent incompressible Navier–Stokes equations. The frequency of vocal fold vibration is set to $f = 100\,\text{Hz}$, corresponding to Strouhal number in the order of $\text{St} = 0.001$. The airflow is driven by a pressure gradient, which mimics physiological conditions

Table 5 Boundary conditions for the velocity $\boldsymbol{v}$ and kinematic pressure $P = p/\rho$. Vector $\boldsymbol{n}$ denotes the unit outer normal, $\boldsymbol{u}$ is the prescribed boundary displacement

$\boldsymbol{v}$ [m/s]			P [m^2/s^2]
G_{in}	evaluated	$(\boldsymbol{v} \cdot \boldsymbol{n} < 0)$	$P + \frac{1}{2}\|\boldsymbol{v}\|^2 = 300$
	$\boldsymbol{v} = 0$	$(\boldsymbol{v} \cdot \boldsymbol{n} > 0)$	
G_{out}	$\partial \boldsymbol{v}/\partial \boldsymbol{n} = 0$	$(\boldsymbol{v} \cdot \boldsymbol{n} > 0)$	$P = 0$
	$\boldsymbol{v} = 0$	$(\boldsymbol{v} \cdot \boldsymbol{n} < 0)$	
G_{VF}^{L}	$\boldsymbol{v} = \frac{\partial \boldsymbol{u}}{\partial t}$		$\frac{\partial P}{\partial \boldsymbol{n}} = 0$
G_{VF}^{U}	$\boldsymbol{v} = \frac{\partial \boldsymbol{u}}{\partial t}$		$\frac{\partial P}{\partial \boldsymbol{n}} = 0$
G_{wall}	$\boldsymbol{v} = 0$		$\frac{\partial P}{\partial \boldsymbol{n}} = 0$

with a constant lung pressure at the inlet and a zero relative pressure at the outlet. The boundary conditions for the velocity $\boldsymbol{v}$ and kinematic pressure $P = p/\rho$ are summarized in Table 5. The Navier–Stokes equations were discretized using a collocated cell-centered variant of the finite volume method for unstructured meshes. The numerical solution was implemented with the help of OpenFOAM. The discretization scheme for the time derivative is first-order Euler implicit, a total variation diminishing (TVD) scheme for the convection term and central differencing with explicit non-orthogonal correction for the diffusion term. The time step Δt is adjusted automatically during the transient solution so that the maximum local Courant number is kept below a predefined limit. In the current simulations, the Courant number was kept below 1, resulting in a time step size Δt of $5 \cdot 10^{-7}$ s–$1.5 \cdot 10^{-6}$ s. The discretized Navier–Stokes equations were solved by a segregated solver based on a modified pressure implicit with splitting of operators (PISO) algorithm (Issa 1986), with the preconditioned biconjugate gradient linear solver for the momentum equations and algebraic multigrid for the pressure equation.

CFD results The results of the CFD simulations are displayed in Fig. 27 in mid-coronal z-normal sections at four time instants corresponding to the closing phase, maximum closure, opening phase and maximum opening. The velocity fields are taken from the 19th period of vibration, when the flow is already fully developed. Figure 28 shows the velocity magnitude in the transverse planes and the jet contours (velocity isosurfaces), giving insight in the three-dimensionality of the supra-glottal flow fields. The CFD results confirm the experimental findings in Triep and Brücker (2010) and numerical simulations in Schwarze et al. (2011), who showed that this geometry promotes the phenomenon of jet axis switching. The jet, mostly planar and aligned along the anterior-posterior axis within glottis, changes its orientation further downstream of the glottis and aligns in the medial-lateral direction in the second half of the opening phase and first half of the closing phase. The axis switching also induces complex 3D vortex structures within the ventricles.

Acoustic model The acoustic domain consists of three parts: The first part is the larynx, which contains the aeroacoustic sources and corresponds to the flow domain. Attached to it is the second part, the vocal tract, which is a 18.25 cm long tube with

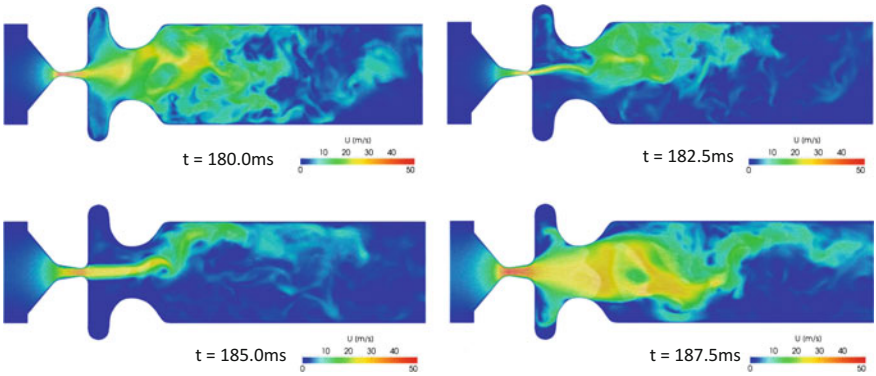

Fig. 27 Velocity magnitude in z-normal (coronal) mid-plane at four time instants during the 19th period of oscillation. From *left* to *right* closing phase, maximum closure, opening phase, maximum opening

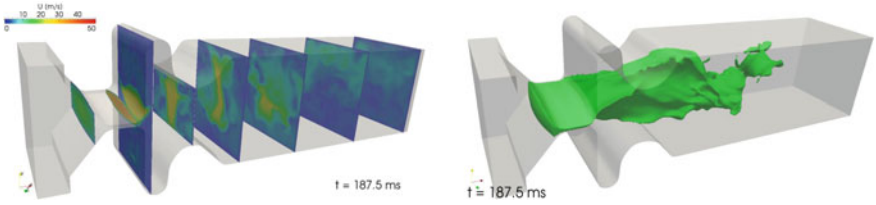

Fig. 28 Velocity magnitude and jet contours (isosurface at $u = 15$ m/s), maximum opening

varying diameter along the center axis. The vocal tract acts as an acoustic filter and modulates the generated sound, by amplifying or reducing the amplitudes at certain frequencies. For this purpose the vocal tract geometry representing the vowel /u/ ("who") was chosen. Exact dimensions were taken from Story et al. (1996), where 18 three-dimensional vocal tract shapes were acquired by means of magnetic resonance imaging (MRI).

The last part of the acoustic domain is the propagation region, a $2.5 \times 2.5 \times 2.5\,\text{cm}^3$ big box, which is added at the end of the vocal tract. Its purpose is to capture the sound wave in 1 cm distance from the mouth at the monitoring position "MIC". In Fig. 29 the geometric model used for the acoustic simulation together with the monitoring point is plotted.

The grid size of the acoustic simulation can be chosen considerably coarser than the characteristic length of the CFD grid (0.15 mm). Therefore the acoustic mesh is composed of hexahedron elements with a characteristic length of 0.2 mm inside the glottis region (corresponds to the CFD domain). The non-conforming grid technique allows us to directly connect the source (flow domain) and propagation domain (corresponds to the vocal tract). The overall grid for the acoustic simulation is fine enough for computations up to 3.5 kHz. All channel walls are considered to be fully reflecting, and perfectly matched layers (PML) are located at the inflow (1 cm in front

of the glottis) and surrounding the propagation region (see Fig. 29). The PML at the inlet is 5 mm long in x-direction and 6 mm in normal direction to the propagation region.

Acoustics results The acoustic field is computed by the FE method solving the perturbed convective wave equation (PCWE) as described in Sect. 5.2. For the acoustic source analysis, the substantial derivative of the incompressible pressure p_{ic} is Fourier transformed over the whole domain. The fundamental frequency is found at 100 Hz, as this is the frequency the vocal folds are being driven. Investigating the acoustic sources show that the main contributions are inside the glottis, as the contour plots in Fig. 30 reveal. Studying the source distribution for a non-harmonic frequency of 2665 Hz, which is a random representative of the broadband spectrum, reveals that the sources are distributed downstream which correlates to the vortex shedding region (see Fig. 28). For other frequencies of the broadband spectrum, the results are comparable, concerning distribution and amplitude of the source region.

The monitoring point "MIC" is situated 1 cm downstream of the mouth, as sketched in Fig. 29. The computed acoustic spectrum is plotted in Fig. 31 and shows

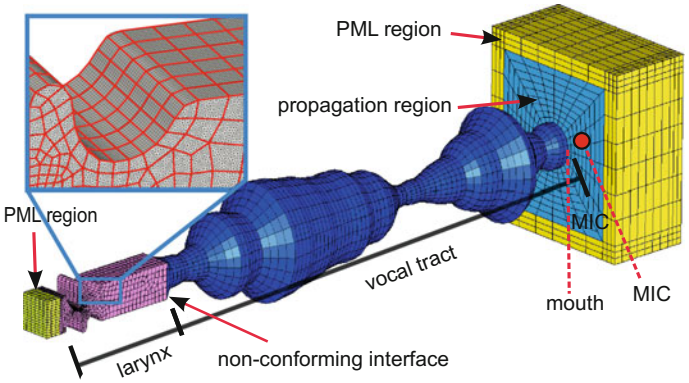

Fig. 29 Geometry and mesh for the acoustic simulation. Larynx, vocal tract, propagation region, perfectly matched layer (PML) regions and comparison of the fine CFD grid and coarse acoustic grid

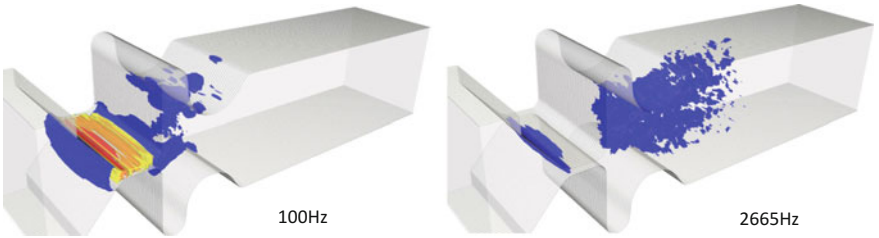

Fig. 30 Acoustic sources at main frequency (100 Hz) and at 2665 Hz

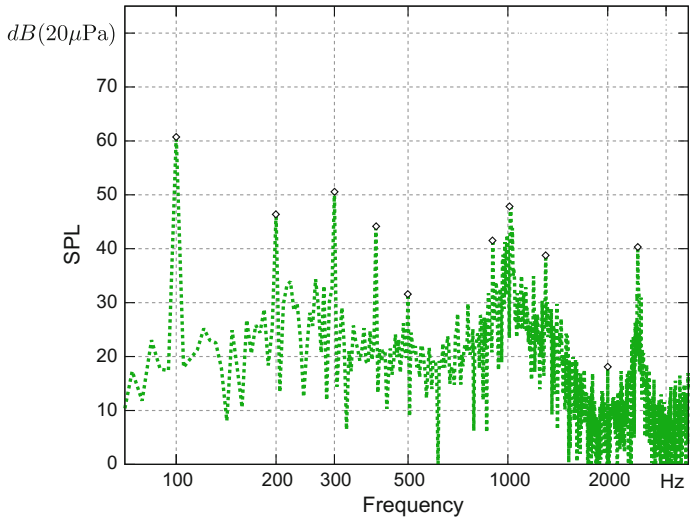

Fig. 31 Acoustic sound spectra at a monitoring point "MIC" for the vocal tract model /u/. Harmonics are emphasized with the symbols ◇

that the first harmonic has the largest amplitude, and all other harmonics are up to 15 dB lower. Furthermore, the amplitudes at non-harmonics are consistently smaller by about 5 dB.

Acknowledgements The author wishes to acknowledge his former Ph.D. students Andreas Hüppe, Simon Triebenbacher and Stefan Zörner for main contributions towards non-conforming grid techniques and its applications. Furthermore, I wish to tanks my colleague Barbara Wohlmuth (Technische Universität München, Germany) for our longtime cooperation on non-conforming grid techniques. Finally, many thanks to Stefan Schoder for proof reading and his usefull suggestions.

References

Alipour, F., Brücker, C., Cook, D., Gömmel, A., Kaltenbacher, M., Willy, M., et al. (2011). Mathematical models and numerical schemes for the simulation of human phonation. *Current Bioinformatics*, *6*(3), 323–343.

Becker, S., Hahn, C., Kaltenbacher, M., & Lerch, R. (2008). Flow-induced sound of wall-mounted cylinders with different geometries. *AIAA Journal*, *46*(9), 2265–2281.

Bernardi, C., Maday, Y., & Patera, A. T. (1994). A new nonconforming approach to domain decomposition: The mortar element method. *Nonlinear partial differential equations and their applications. Collège de France Seminar, Vol. XI (Paris, 1989–1991)* (Vol. 299, pp. 13–51). Pitman research notes in mathematics series. Harlow: Longman Scientific and Technical.

Dokeva, N. (2006). Scalable mortar methods for elliptic problems on many subregions. Ph.D. thesis, University of Southern California.

Döllinger, M., Kobler, J., Berry, A., Mehta, D., Luegmair, G., & Bohr, C. (2011). Experiments on analysing voice production: Excised (human, animal) and in vivo (animal) approaches. *Current Bioinformatics*, *6*(3), 286–304.

Donea, J., Huerta, A., Ponthot, J. P., & Rodriguez-Ferran, A. (2004). Arbitrary Lagrangian-Eulerian methods. *Encyclopedia of computational mechanics*. New York: Wiley.

Durst, F., & Schäfer, M. (1996). A parallel block-structured multigrid method for the prediction of incompressible flows. *International Journal for Numerical Methods in Fluids*, *22*, 549–565.

Escobar, M. (2007). Simulation of flow induced noise. Ph.D. thesis, Department of Sensor Technology, University of Erlangen-Nuremberg.

Ewert, R., & Schröder, W. (2003). Acoustic perturbation equations based on flow decomposition via source filtering. *Journal of Computational Physics*, *188*, 365–398.

Farrell, P. E., & Maddison, J. R. (2011). Conservative interpolation between volume meshes by local Galerkin projection. *Computer Methods in Applied Mechanics and Engineering*, *200*, 89–100.

Flemisch, B., Kaltenbacher, M., Triebenbacher, S., & Wohlmuth, B. (2012). Non-matching grids for a flexible discretization in computational acoustics. *Communications in Computational Physics*, *11*(2), 472–488.

Fritz, A., Hüeber, S., & Wohlmuth, B. (2004). A comparison of mortar and Nitsche techniques for linear elasticity. In *CALCOLO*.

Gander, M. J., & Japhet, C. (2009). An algorithm for non-matching grid projections with linear complexity. *Domain decomposition methods in science and engineering XVIII*. Berlin: Springer.

Grabinger, J. (2007). Mechanical-acoustic coupling on non-matching finite element grids. Master's thesis, University Erlangen-Nuremberg.

Greiner, G., & Hormann, K. (1998). Efficient clipping of arbitrary polygons. *ACM Transactions on Graphics*, *17*, 71–83.

Hahn, C. (2008). Experimentelle Analyse und Reduktion aeroakustischer Schallquellen an einfachen Modellstrukturen. Ph.D. thesis, University of Erlangen-Nuremberg.

Hansbo, A., Hansbo, P., & Larson, M. G. (2003). A finite element method on composite grids based on Nitsche's method. *ESAIM: Mathematical Modelling and Numerical Analysis*, *37*(3), 495–514.

Hardin, J. C., & Pope, D. S. (1994). An acoustic/viscous splitting technique for computational aeroacoustics. *Theoretical and Computational Fluid Dynamics*, *6*, 323–340.

Heinstein, M. W., & Laursen, T. A. (2003). Consistent mesh tying methods for topologically distinct discretized surfaces in non-linear solid mechanics. *International Journal for Numerical Methods in Engineering*, *57*, 1197–1242.

Hughes, T. J. R. (2000). *The finite element method*. New York: Dover.

Hüppe, A. (2013). Spectral finite elements for acoustic field computation. Ph.D. thesis, University of Klagenfurt, Austria.

Issa, R. I. (1986). Solution of the implicitly discretised fluid flow equations by operator-splitting. *Journal of Computational Physics*, *62*(1), 40–65.

Kaltenbacher, B., Kaltenbacher, M., & Sim, I. (2013). A modified and stable version of a perfectly matched layer technique for the 3-d second order wave equation in time domain with an application to aeroacoustics. *Journal of Computational Physics*, *235*, 407–422.

Kaltenbacher, M. (2015). *Numerical simulation of mechatronic sensors and actuators - finite elements for computational multiphysics* (3rd ed.). Berlin: Springer.

Kaltenbacher, M., Escobar, M., Ali, I., & Becker, S. (2010). Numerical simulation of flow-induced noise using LES/SAS and Lighthill's acoustics analogy. *International Journal for Numerical Methods in Fluids*, *63*(9), 1103–1122.

Kaltenbacher, M., Hüppe, A., Grabinger, J., & Wohlmuth, B. (2016a). Modeling and finite element formulation for acoustic problems including rotating domains. *AIAA Journal*, *54*, 3768–3777.

Kaltenbacher, M., Hüppe, A., Reppenhagen, A., Tautz, M., Becker, S., & Kühnel, W. (2016b). Computational aeroacoustics for HVAC systems utilizing a hybrid approach. *SAE International*, *9*.

Kelleher, J. E., Siegmund, T., Du, M., Naseri, E., & Chan, R. W. (2013). Empirical measurements of biomechanical anisotropy of the human vocal fold lamina propria. *Biomechanics and Modeling in Mechanobiology*, *12*(3), 555–567.

Klöppel, T., Popp, A., Küttler, U., & Wall, W. (2011). Fluid - structure interaction for non-conforming interfaces based on a dual morta formulation. *Computer Methods in Applied Mechanics and Engineering*, *200*(45), 3111–3126.

Köck, H., Eisner, S., & Kaltenbacher, M. (2015). Electrothermal multiscale modeling and simulation concepts for power electronics. *IEEE Transactions on Power Electronics*, *99*.

Langer, U., & Steinbach, P. (2003). Boundary element tearing and interconnecting methods. *Computing*, *71*(3), 205–228.

Link, G., Kaltenbacher, M., Breuer, M., & Dllinger, M. (2009). A 2d finite-element scheme for fluidsolidacoustic interactions and its application to human phonation. *Computer Methods in Applied Mechanics and Engineering*, *198*, 3321–3334.

Menter, F., & Egorov, Y. (2005). A scale adaptive simulation model using two-equation models. In *43rd AIAA Aerospace Sciences Meeting and Exhibit*, number AIAA-2005-1095.

Munz, C. D., Dumbser, M., & Roller, S. (2007). Linearized acoustic perturbation equations for low Mach number flow with variable density and temperature. *Journal of Computational Physics*, *224*, 352–364.

Park, K. C., & Felippa, C. A. (2002). A simple algorithm for localized construction of non-matching structural interfaces. *International Journal for Numerical Methods in Engineering*, *53*, 2117–2142.

Puso, M. A. (2004). A 3d mortar method for solid mechanics. *International Journal for Numerical Methods in Engineering*, *59*, 315–336.

Puso, M. A., & Laursen, T. A. (2002). A 3d contact smoothing method using Gregory patches. *International Journal for Numerical Methods in Engineering*, *54*, 1161–1194.

Schwarze, R., Mattheus, W., Klostermann, J., & Brücker, C. (2011). Starting jet flows in a three-dimensional channel with larynx-shaped constriction. *Computers and Fluids*, *48*(1), 68–83.

Seo, J. H., & Mittal, R. (2011). A high-order immersed boundary method for acoustic wave scattering and low-Mach number flow-induced sound in complex geometries. *Journal of Computational Physics*, *230*(4), 1000–1019.

Seo, J. H., & Moon, Y. J. (2005). Perturbed compressible equations for aeroacoustic noise prediction at low Mach numbers. *AIAA Journal*, *43*, 1716–1724.

Shen, W. Z., & Sørensen, J. N. (1999). Aeroacoustic modelling of low-speed flows. *Theoretical and Computational Fluid Dynamics*, *13*, 271–289.

Šidlof, P., Zörner, S., & Hüppe, A. (2014). A hybrid approach to the computational aeroacoustics of human voice production. *Biomechanics and Modeling in Mechanobiology*, 1–16.

Spalart, P. R., & Allmaras, S. R. (1994). A one-equation turbulence model for aerodynamic flows. *Recherche Aerospatiale*, *1*, 5–21.

Story, B. H., Titze, I. R., & Hoffman, E. A. (1996). Vocal tract area functions from magnetic resonance imaging. *The Journal of the Acoustical Society of America*, *100*(1), 537–554.

Svec, J., & Schutte, H. K. (2012). Kymographic imaging of laryngeal vibrations. *Current Opinion in Otolaryngology and Head and Neck Surgery*, *20*(6), 458–465.

Triep, M., & Brücker, C. (2010). Three-dimensional nature of the glottal jet. *The Journal of the Acoustical Society of America*, *127*(3), 1537–1547.

Wohlmuth, B. I. (2000). A mortar finite element method using dual spaces for the Lagrange multiplier. *SIAM Journal on Numerical Analysis*, *38*(3), 989–1012.

Zörner, S., Kaltenbacher, M., Lerch, R., Sutor, A., & Döllinger, M. (2010). Measurement of the elasticity modulus of soft tissues. *Journal of Biomechanics*, *43*(8), 1540–1545.

Zörner, S., Kaltenbacher, M., & Döllinger, M. (2013). Investigation of prescribed movement in fluid-structure interaction simulation for the human phonation process. *Computers and Fluids*, *86*, 133–140.

http://www.springer.com/978-3-319-59037-0

Computational Acoustics
Kaltenbacher, M. (Ed.)
2018, VII, 251 p. 122 illus., 89 illus. in color., Hardcover
ISBN: 978-3-319-59037-0